INTERNATIONAL JOURNAL FOR NUMERICAL METHODS IN FLUIDS, VOL. 21, 1067–1086 (1995)

A SEGREGATED IMPLICIT SOLUTION ALGORITHM FOR 2D AND 3D LAMINAR INCOMPRESSIBLE FLOWS

K. C. GIANNAKOGLOU AND E. S. POLITIS

Laboratory of Thermal Turbomachines, National Technical University of Athens, PO Box 64069, Athens 15710, Greece

SUMMARY

A segregated algorithm for the solution of laminar incompressible, two- and three-dimensional flow problems is presented. This algorithm employs the successive solution of the momentum and continuity equations by means of a decoupled implicit solution method. The inversion of the coefficient matrix which is common for all momentum equations is carried out through an approximate factorization in upper and lower triangular matrices. The divergence-free velocity constraint is satisfied by formulating and solving a pressure correction equation. For the latter a combined application of a preconditioning technique and a Krylov subspace method is employed and proved more efficient than the approximate factorization method. The method exhibits a monotonic convergence, it is not costly in CPU time per iteration and provides accurate solutions which are independent of the underrelaxation parameter used in the momentum equations. Results are presented in two- and three-dimensional flow problems.

KEY WORDS: laminar flows; incompressible flows; pressure correction; Krylov subspace methods; approximate factorization

1. INTRODUCTION

Laminar incompressible flows appearing in engineering and biomedical systems are typical test cases for validating Navier–Stokes solution methods. Finite-volume methods in curvilinear grid systems are widely used to discretize the flow equations. Depending on how the continuity equation is implemented, artificial compressibility[1] or pressure correction[2,3] technique are used.

The present method is based on the SIMPLE algorithm[4] which was originally developed for staggered grid arrangements. Aiming at a wider flexibility in the analysis of complex geometries, the collocated grid arrangement is adopted in this paper at the expense of a procedure which circumvents velocity–pressure decoupling. Both two- and three-dimensional domains are discretized using body-fitted curvilinear co-ordinates, where all flow variables are stored at the centres of the computational cells. The method is capable of handling non-orthogonal grids even though orthogonal curvilinear ones are used in most of the examined cases. The exact pressure correction equation is written at each cell centre and is extended over the cell faces under physically reasonable assumptions. This allows the expression of the contravariant velocity components at cell faces through a wider pressure molecule (in conformity with the original scheme of Rhie and Chow[5]), which prevents decoupling between velocity and pressure fields. This analysis, combined with appropriate numerical schemes, leads to a fast convergence of the continuity equation and a smooth solution field which is independent of the underrelaxation factor used in the momentum equations.

From a numerical point of view the elliptic character of the governing equations is retained and a segregated solution algorithm is established in conjunction with fast elliptic solvers. The two (for 2D problems) or three (for 3D problems) momentum equations are solved by applying the modified

CCC 0271–2091/95/111067–20
© 1995 by John Wiley & Sons, Ltd.
Received November 1994
Revised April 1995

strongly implicit procedure (MSIP)[6] for scalar equations. This is carried out at the expense of a single factorization of the common coefficient matrix resulting from the discretization of the momentum equations. The pressure corrrection equation is solved at the end of each iteration using a minimization algorithm for the preconditioned residual of the continuity equation. This algorithm is a degenerate variant of the restarted generalized minimal residual technique[7] and could be referred to as GMRES(1). For the pressure correction equation this scheme was proved more efficient than the typical MSIP solver. The proposed algorithm exhibits a monotonic, although slightly wavy, convergence.

The assessment of the proposed method will be demonstrated through a number of two- and three-dimensional laminar flow problems. Useful conclusions are drawn about (a) the convergence properties of the segregated algorithm, (b) the comparative behaviour of the two numerical solvers used for the pressure correction equation, (c) the advantages as well as the additional cost of using a full discretization molecule (including non-orthogonal terms) in the pressure correction equation and (d) the role of underrelaxation in the momentum and continuity equations.

2. GOVERNING EQUATIONS

Governing equations will be presented in the case of three-dimensional flows. Steady incompressible fluid motion is governed by the continuity and the momentum conservation equations, which can be written in a Cartesian co-ordinate system (x_i, $i = 1, 2, 3$) as

$$\frac{\partial u_j}{\partial x_j} = 0, \tag{1}$$

$$\frac{\partial}{\partial x_j}(u_i u_j) = -\frac{\partial p}{\partial x_i} + \frac{\partial}{\partial x_j}\left[\nu\left(\frac{\partial u_i}{\partial x_j} + \frac{\partial u_j}{\partial x_i}\right)\right], \quad i = 1, 2, 3, \tag{2}$$

where u_i, $i = 1, 2, 3$, are the three Cartesian velocity components and ν is the kinematic viscosity of the fluid. A repeated index denotes summation over the three spatial components. When a body-fitted curvilinear co-ordinate system is introduced, new independent variables (ξ^i, $i = 1, 2, 3$) appear and equations (1) and (2) need to be transformed accordingly. If J is the Jacobian of the transformation, i.e.

$$J = \frac{\partial(x_1, x_2, x_3)}{\partial(\xi^1, \xi^2, \xi^3)}, \tag{3}$$

the aforementioned equations can be cast in the form

$$\frac{\partial}{\partial \xi^j}(JV^j) = 0, \tag{4}$$

$$\frac{\partial}{\partial \xi^j}(JV^j u_i) = \frac{\partial}{\partial \xi^j}\left(J\nu g^{jk}\frac{\partial u_i}{\partial x_k}\right) - J\frac{\partial p}{\partial x_i}, \quad i = 1, 2, 3, \tag{5}$$

where g^{jk} is the contravariant metric tensor of the transformation and $V^j, j = 1, 2, 3$ stand for the contravariant velocity components. These are expressed as the inner product of the Cartesian velocity vector and the contravariant base vectors, namely

$$V^j = \vec{V} \cdot \vec{g}^j, \quad j = 1, 2, 3, \tag{6}$$

where

$$\vec{g}^j = \nabla \xi^j, \quad j = 1, 2, 3. \tag{7}$$

In equation (5) the pressure gradient term is retained in its Cartesian form for reasons that will become clear in a later section where the pressure correction algorithm is discussed. It is also to be said that p stands for the static pressure divided by the density, which remains constant all over the flow field.

3. DISCRETIZATION

In this section the application of a finite volume technique for the discretization of the governing equations will be presented. This will be done in the general, three-dimensional, flow case, the two-dimensional one being so straightforward that the reader could work it himself. The computational cells consist of volumes defined by eight neighbouring grid nodes. All flow variables are stored at the centres of these cells and, apart from the Cartesian velocity components, linear interpolations are used for the calculation of any other flow quantity at the centres of the six faces. Figure 1 illustrates such a computational cell and conveys to the reader the main notation used in the present analysis.

Equations (5) are integrated by applying the Gauss theorem over the control volume surrounding any node P at which the flow quantities are stored. This integration leads to the balance of the momentum fluxes at the six faces of the control volume and the body forces acting on the control volume. The fluxes at cell faces involve both convective and diffusive terms and the momentum equation, written for the ith Cartesian velocity component, yields

$$\left[Jvg^{11}\frac{\partial u_i}{\partial \xi^1} - JV^1 u_i\right]_w^e + \left[Jvg^{22}\frac{\partial u_i}{\partial \xi^2} - JV^2 u_i\right]_s^n + \left[Jvg^{33}\frac{\partial u_i}{\partial \xi^3} - JV^3 u_i\right]_b^f = JP_i + C_i, \quad i = 1, 2, 3, \tag{8}$$

where P_i, $i = 1, 2, 3$, stand for the integrals of the pressure gradient terms and C_i summarize the cross-diffusion terms which involve the metric quantities g^{ij} $(i \neq j)$. The terms C_i can be treated either explicitly or implicitly. Depending on how these terms are handled, the discretized momentum equations involve seven (if C_i are treated explicitly) or 19 neighbouring nodes. The case of a 19-node molecule will not, however, be elaborated in this section in the interest of space. The seven-node discretization scheme reads

$$\sum_{k=\mathrm{E,W,N,S,F,B}} A_k u_i^k - A_\mathrm{P} u_i^\mathrm{P} + S_i = 0, \quad i = 1, 2, 3, \tag{9}$$

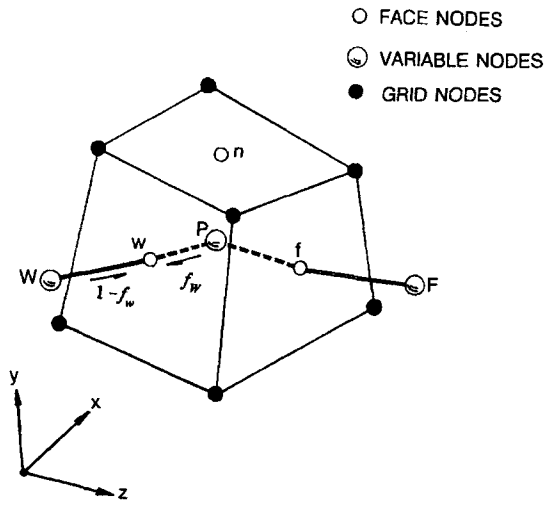

Figure 1. Three-dimensional control volume in the physical space and relevant notation

where A_P is the central node coefficient and the superscripts on the dependent variables u_i denote the nodes where these are referred to.

The finite difference coefficients depend on the convective velocities, the metrics of the transformation and the discretization schemes used. Central differences for the diffusion and three different discretization schemes for the convection terms were programmed and tested, namely

(a) the first-order upwind scheme, with enhanced stability properties at the expense of accuracy, where the convected quantities at the mid-faces of any control volume are set equal to their values at the centre of the upwind cell[8]
(b) the hybrid upwind/central scheme,[9] which is identical with the central scheme when the absolute value of the local Peclet number (for each velocity component at the cell faces) is less than two; otherwise the scheme reduces to the first-order upwind scheme with zero diffusion terms
(c) the QUICK scheme,[10] which employs a three-point upstream-weighted quadratic interpolation technique; in this work the consistently formulated QUICK scheme of Hayase *et al.*[11] is used, which introduces additional source terms lumped in the RHS part of equation (8).

It must be pointed out that the three momentum equations share the same finite difference coefficient matrix $[A]$. Thus for the solution of the three momentum equations a single matrix inversion is required, diminishing the computational time.

In the course of the iterative algorithm the numerical solution of the momentum equations provides an intermediate velocity field u_i^*, $i=1, 2, 3$, which in general does not satisfy the continuity equation. Following the pressure correction concept,[4] both pressure and velocities are corrected according to the expressions

$$u_i^{(n+1)} = u_i^* + u_i', \quad i = 1, 2, 3, \tag{10a}$$

$$p^{(n+1)} = p^{(n)} + p', \tag{10b}$$

where superscripts in parentheses stand for the iteration level. We recall that the intermediate velocity field u_i^*, $i=1, 2, 3$, is the outcome of the solution of (9) at the geometrical centres of the control volumes. It is also to be said that equations (9) are underrelaxed by means of a factor ω and read

$$u_i^{P*} = \frac{\omega}{A_P} \sum_{k=E,W,N,S,F,B} A_k u_i^{k*} - \frac{\omega}{A_P} J \frac{\partial p}{\partial x_i} + \frac{\omega}{A_P} C_i + (1-\omega) u_i^{P(n)}, \quad i = 1, 2, 3. \tag{11}$$

In order to formulate the pressure correction equation, it is assumed that equation (11) is also valid at the centres of the cell faces. At the same locations the contravariant velocity components must be calculated since they are involved in the continuity equation; this is performed on the basis of equation (11). Let m be any face centre lying between the central node P and the neighbouring one M. A rearrangement of terms in (11) leads to the following expression for the contravariant velocity component V_m^π ($\pi = 1, 2, 3$) normal to the corresponding face:

$$(V^\pi)_m^* = \frac{\omega}{A_m} \left\{ \sum_k A_k u_i^{k*} \frac{\partial \xi^\pi}{\partial x_i} \right\}_m - J_m \frac{\omega}{A_m} \left\{ \frac{\partial p}{\partial \xi^j} \frac{\partial \xi^j}{\partial x_i} \frac{\partial \xi^\pi}{\partial x_i} \right\}_m + \frac{\omega}{A_m} \left\{ C_i \frac{\partial \xi^\pi}{\partial x_i} \right\}_m + (1-\omega)(V^\pi)_m^{(n)}, \quad \pi = 1, 2, 3. \tag{12}$$

The last term in equation (12) is treated explicitly in order to prevent any dependence of the solution on the underrelaxation factor ω. Velocity–pressure decoupling is overcome by means of a centred finite difference analysis of the pressure gradient term in (12). Assumptions are to be made about how quantities involved in (11) are transferred to the cell faces, namely

$$\frac{\left(\sum_k A_k u_i^{k*}\right)_m}{A_m} = \frac{\left(\sum_k A_k u_i^{k*}\right)_P}{A_P} f_M + \frac{\left(\sum_k A_k u_i^{k*}\right)_M}{A_M}(1 - f_M), \quad 1, 2, 3, \tag{13a}$$

$$\frac{(C_i)_m}{A_m} = \frac{(C_i)_P}{A_P} f_M + \frac{(C_i)_M}{A_M}(1 - f_M), \quad i = 1, 2, 3, \tag{13b}$$

$$\frac{1}{A_m} = \frac{1}{A_P} f_M + \frac{1}{A_M}(1 - f_M), \tag{13c}$$

where f_M is an interpolation coefficient used for the calculation of any scalar quantity at the point m from its values at the surrounding nodes P and M. Assumptions (13) are in accordance with the momentum interpolation scheme of Majumdar,[12] although in the present method the whole pressure gradient term is retained.

In order not to damage the already satisfied momentum equations, it is proposed that the pressure and (contravariant) velocity corrections introduced in (10) must be linked through the relation

$$(V^\pi)'_m = -J_m \frac{\omega}{A_m}\left[\frac{\partial p'}{\partial \xi^j}\frac{\partial \xi^j}{\partial x_i}\frac{\partial \xi^\pi}{\partial x_i}\right]_m, \tag{14a}$$

which also holds for any integer node in the form

$$(u_i^P)' = -J \frac{\omega}{A_P}\left[\frac{\partial p'}{\partial \xi^i}\frac{\partial \xi^j}{\partial x_\lambda}\frac{\partial \xi^k}{\partial x_\lambda}\frac{\partial x_i}{\partial \xi^k}\right]_P. \tag{14b}$$

The pressure correction equation is merely formed by requiring that the corrected velocity components satisfy the divergence-free constraint. It can be written in the standard form

$$\sum_k B_k p'_k - B_P p'_P + S^* = 0, \tag{15}$$

where the source term S^* stands for the non-zero divergence of the provisional velocity field u_i^*, $i = 1, 2, 3$. In equation (15) k runs over either six or 18 neighbouring nodes of P. If the reduced seven-node molecule is used, equation (14) is further simplified by neglecting all cross-metrics. The use of a complete discretization molecule, which accounts for 19 nodes, is meaningful in cases of non-orthogonal grids[13] and usually decreases the number of iterative steps required, with the offset of additional CPU time per iteration.

4. NUMERICAL SCHEMES

After discretizing the governing equations, the linearized momentum and the pressure correction equations can be expressed in matrix form as

$$[A]\vec{q} = \vec{b}. \tag{16}$$

As mentioned above, all three momentum equations share the same coefficient matrix $[A]$ and consequently a single inversion of $[A]$ is required.

The proposed solution algorithm is an iterative one based on the successive solution of the discretized equations through implicit schemes. The following steps are identified.

Step 1. Calculation of $[A]$ by discretizing the momentum equations.
Step 2. Approximate inversion of matrix $[A]$.
Step 3. Successive solution of the three momentum equations using the same implicit scheme for all equations. An intermediate velocity field, which in general fails to satisfy the divergence-free constraint, is calculated.
Step 4. Calculation and approximate inversion of matrix $[B]$ for the pressure correction equation.
Step 5. Solution of the pressure correction equation using an implicit scheme.
Step 6. Velocities and pressure are updated at the cell centres. In the same step the contravariant velocities at the control volume faces are also updated and stored.

Aiming at the optimum convergence rate, two different numerical schemes for the solution of the pressure correction equation (Step 5) were implemented and tested. These will be referred to as Solvers P1 and P2 and are analysed below. With regard to the momentum equations the same implicit solution method (Solver P1) was exclusively used. For the sake of simplicity the model equation (16) will be analysed herein, with $[A]$ standing for $[A]$ or $[B]$ accordingly.

The first solution scheme (Solver P1) is the modified strongly implicit procedure.[6] According to the MSIP, $[A]$ is approximately decomposed into an upper and a lower triangular matrix, i.e.

$$[A] \approx [P] = [L][U], \tag{17}$$

using a recursive algorithm. Matrices $[L]$ and $[U]$ have the same structure as the lower and upper parts of $[A]$ respectively. In forming $[L]$ and $[U]$, a parameter α (usually $\alpha = 0{\cdot}3$–$0{\cdot}5$) is employed so that the $[L][U]$ product is as close as possible to the original matrix $[A]$. Numerical tests demonstrated the insensitivity of the convergence rate to the value of α.

In the first 2D flow problem examined, the MSIP was applied for both the five-node and the nine-node (full-stencil) finite difference discretization of (16). A comparative study of the two formulations is carried out and discussed. It must be pointed out that the overhead in computational cost of the full-stencil factorization is important only in 3D applications.

The second solution scheme (Solver P2) is based on a combined application of a preconditioning technique and a Krylov subspace method. Solver P2 shares the features of the restarted generalized minimum residual algorithm[7] using the MSIP as preconditioner. An equivalent problem to (16) is formed where the preconditioned residual

$$\vec{R}^{(n)} = [P]^{-1}([A]\vec{q}^{(n)} - \vec{b}^{(n)}) \tag{18}$$

is minimized. In equation (18) $[P]$ is an easily invertible approximation of $[A]$ and as such the factorization (17) is used. In order to advance the solution from iteration (n) to iteration $(n+1)$, the preconditioned residual multiplied by an acceleration parameter β is added to the existing solution vector $\vec{q}^{(n)}$ according to the expression

$$\vec{q}^{(n+1)} = \vec{q}^{(n)} + \beta\vec{R}^{(n)}. \tag{19}$$

The calculation of β is based on the minimization of the preconditioned residual at the next iteration $(n+1)$ and its final expression is given as

$$\beta = -\frac{\alpha_1}{\alpha_1^2 + \alpha_2^2}, \tag{20}$$

where

$$\alpha_1 = \vec{\gamma} \cdot \frac{\vec{R}^{(n)}}{\|\vec{R}^{(n)}\|}, \tag{21a}$$

$$\alpha_2 = \left\| \vec{\gamma} - \alpha_1 \frac{\vec{R}^{(n)}}{\|\vec{R}^{(n)}\|} \right\|, \tag{21b}$$

$$\vec{\gamma} = [P]^{-1}[A] \frac{\vec{R}^{(n)}}{\|\vec{R}^{(n)}\|}. \tag{21c}$$

Expressions (21) result from the application of the Arnoldi procedure as used in the restarted GMRES(1) algorithm.[7] According to equation (21c), vector $\vec{\gamma}$ is calculated through the following two-step procedure.

Step 1

$$[L]\vec{\gamma}' = [A] \frac{\vec{R}^{(n)}}{\|\vec{R}^{(n)}\|}.$$

Step 2

$$[U]\vec{\gamma} = \vec{\gamma}'.$$

The difference between Solvers P1 and P2 can be better understood if the equivalent expression to (19) is written for the MSIP as well, which reads

$$\vec{q}^{(n+1)} = \vec{q}^{(n)} - \vec{R}^{(n)}. \tag{22}$$

From the comparison of equations (19) and (22) and the definition of the acceleration parameter β it is evident that Solver P2 employs a weighted, over the whole field, correction to the current values of the dependent variables. This was proved more efficient, mainly during the early phases of the computation when the effects of the arbitrary initialization need to be dumped. It is also evident that the numerical scheme (19) is a Newton-like procedure.

5. RESULTS

5.1. Laminar flow in a channel with a smooth expansion

The first problem examined herein is the laminar flow in a symmetric channel with a smooth expansion, proposed by P. Roache in the Workshop of the IAHR Working Group on Refined Modelling of Flow.[14] The shape of the two-dimensional channel depends on the flow Reynolds number; the lower side-wall of the channel is defined through the expression

$$y(x) = 1 - \frac{1}{2}\left[\tanh\left(2 - \frac{30x}{Re}\right) - \tanh(2)\right], \quad 0 < x < Re/3.$$

In the present paper two flow cases are examined, which correspond to Reynolds numbers equal to 10 and 100, using two different computational grids. The geometry and inlet flow conditions define a symmetric flow problem and only half of the channel is discretized. The geometry and computational grid for the $Re = 10$ case, consisting of 41×31 nodes, are presented in Figure 2. Since the total channel length is equal to $Re/3$, the flow domain corresponding to the $Re = 100$ case is much longer

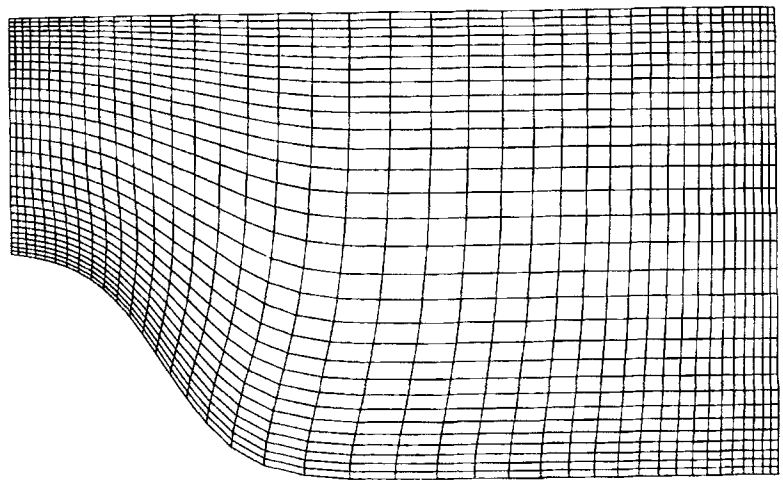

Figure 2. Quasi-orthogonal computational grid for the channel with a smooth expansion ($Re = 10$)

and a finer grid with 93 × 31 nodes was used. Both grids were made quasi-orthogonal by means of an elliptic grid generator incorporating appropriate source terms which control the distribution of grid lines.

At the inlet a fully developed velocity profile is imposed which reads

$$u(y) = 3\left(y - \frac{y^2}{2}\right), \quad 0 \leqslant y \leqslant 1, \qquad v(y) = 0,$$

where the co-ordinate y is zero at the lower point of the inlet cross-section. The inlet pressure is calculated through a zero-derivative condition. Along the symmetry line, symmetry boundary conditions are applied, while zero pressure is defined at the exit.

In Figures 3 and 4, results for the two test cases in the form of pressure and vorticity distributions along the lower solid wall are presented. The pressure distribution over the grid nodes lying along the solid wall is obtained by extrapolating the cell-centred values in the direction normal to the wall. As far as the wall vorticity is concerned, it is obtained through a one-sided, second-order finite difference scheme using the interpolated velocity components over the grid nodes. The calculated distributions are compared with Cliffe *et al.*'s predictions[15] which have been considered as the reference solution. The pressure distributions shown in these figures are normalized, so that a zero wall pressure is obtained at half the channel length. Excellent agreement between the calculated and Cliffe *et al.*'s results can be observed.

The $Re = 10$ case was also chosen for the comparison of the two numerical algorithms proposed for the solution of the pressure correction equation. Calculations were performed using the modified strongly implicit procedure (Solver P1) and the preconditioned minimal residual technique (Solver P2). Figure 5 illustrates the convergence history of the pressure equation for the two aforementioned solution methods. In both cases the incomplete LU decomposition (Solver P1) was used for the solution of the momentum equations. Solver P2 is more efficient in terms of convergence rate (when the iteration number is used as abscissa), so its implementation in the solution of the pressure correction equation is recommended. In fairness, Solver P2 is more time-consuming (per iteration) than Solver P1, but even if this difference is taken into consideration, it still remains more efficient than P1 on the basis of the same convergence tolerance.

The comparison of the two solvers was based exclusively on the pressure correction equation, where differences are more pronounced. The momentum equation in the primitive flow direction (x-

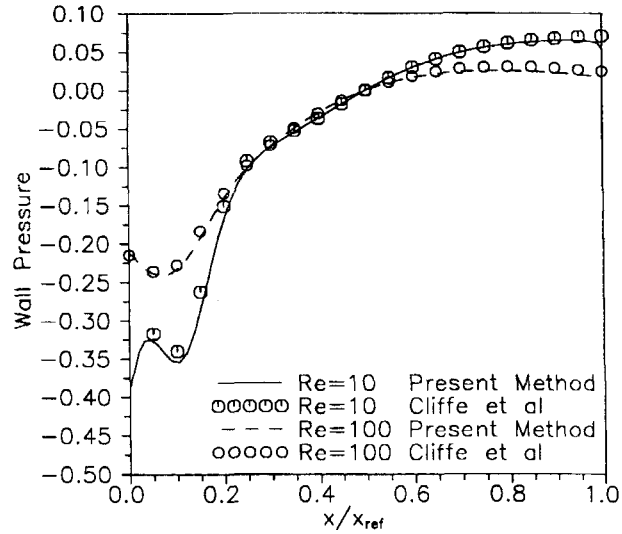

Figure 3. Wall pressure distribution for the channel with a smooth expansion for $Re = 10$ and 100

component) exhibits a similar convergence behaviour, while the y-momentum equation is quite insensitive to the pressure correction solver. For all equations the convergence rate is monotonic in the general sense. The convergence curves are wavy, however, around a mean descending straight line owing to the decoupling of equations. This waviness can be partially attenuated via optimum relaxation factors. Qualitatively similar results and conclusions can be drawn when the $Re = 100$ case is used instead.

For the studies discussed so far, the discretized momentum and pressure correction equations involved five coefficients, namely the central node and its four closest neighbours. Any contribution from the discretized non-orthogonal cross-terms was treated explicitly by lumping it into their right-hand side. In order to investigate the relative advantages of using a nine-entry coefficient matrix in the

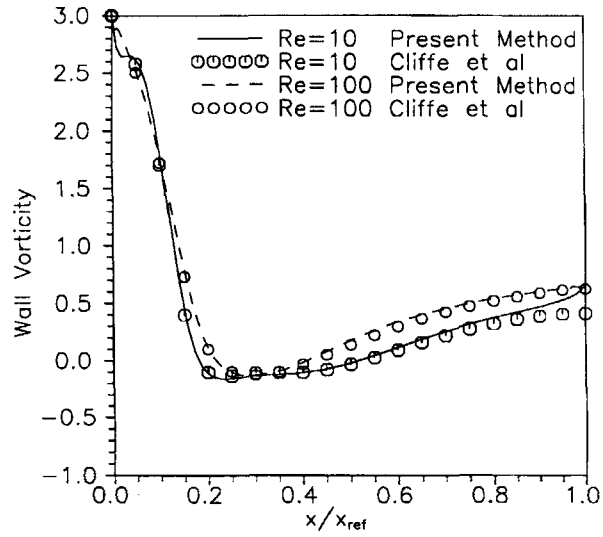

Figure 4. Wall vorticity distribution for the channel with a smooth expansion for $Re = 10$ and 100

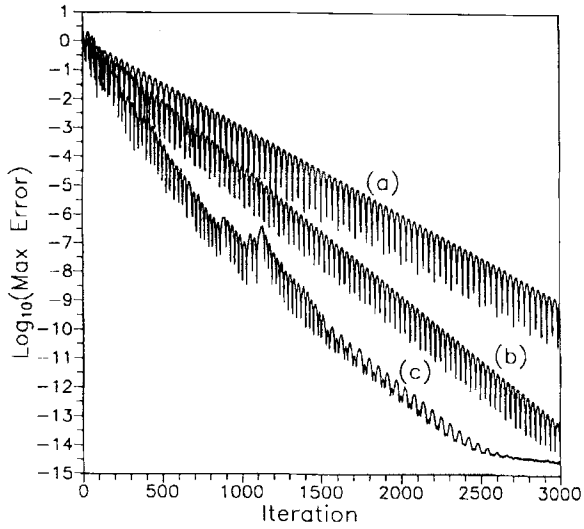

Figure 5. Convergence history for the pressure correction equation, $Re = 10$: (a) Solver P1 (five node molecule); (b) P2 (five-node); (c) P2 (nine-node)

pressure correction equation, an intentionally non-orthogonal grid was built. The $Re = 10$ case was re-examined using both discretization schemes and Solver P2 for the pressure correction equation. The convergence history of the continuity equation for nine-point discretization is also included in Figure 5. As expected, the nine-coefficient discretization leads to a faster convergence rate in terms of iterations. However, this difference in convergence rate does not account for the real difference in computational time required, since the factorization of the nine-entry matrix is approximately 30% slower.

All runs were carried out using an underrelaxation factor $\omega = 0{\cdot}50$ for the momentum equations. No relaxation factor was implemented in the pressure correction equation.

5.2. *Steady flow past a cylinder*

The second two-dimensional flow problem examined is the steady flow past a cylinder at Reynolds numbers (based on the diameter d) ranging from 20 to 100. It is known[16] that steady solutions for the flow around a cylinder become experimentally unstable for Reynolds numbers greater than 40. On the other hand the $Re = 100$ case seems to be the upper limit for which steady fields can be reliably determined by solving the complete flow domain around the cylinder.[17] In the literature there are a few papers reporting solutions for Reynolds numbers greater than 100 by imposing symmetry conditions along the split line which emanates from the back stagnation point; this is an artifice which increases the stability of the solution procedure. In the present study the complete domain around the circular section was numerically modelled using an O-type mesh. The external radius of the 101 × 101 O-type grid used for the $Re = 20$ and 40 cases was $25d$; for the $Re = 100$ case the external radius of the grid was $50d$ and 151 nodes were placed in the radial direction.

Vorticity and pressure coefficient distributions along the cylinder surface for $Re = 20$, 40 and 100 are shown in Figures 6 and 7 respectively. The pressure coefficient is defined as

$$c_p = \frac{p - p_t}{\frac{1}{2}\rho V_{inf}^2}$$

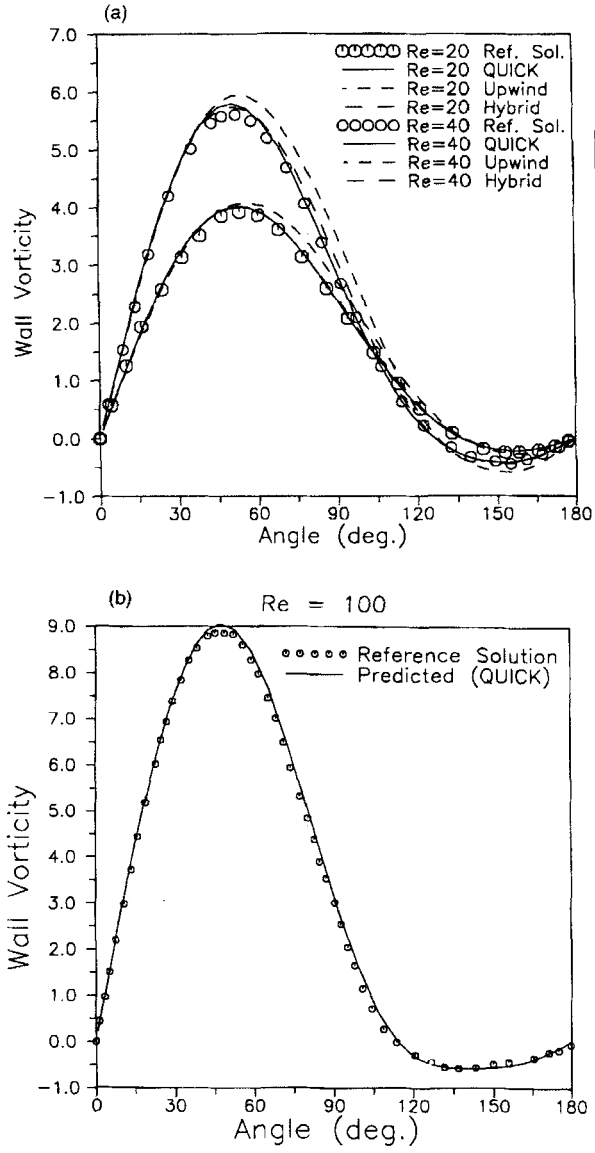

Figure 6. Vorticity distribution along the cylinder surface: (a) $Re = 20$ and 40; (b) $Re = 100$

where p_t is the pressure at the front stagnation point and V_{inf} is the infinite velocity. The results are compared with computational results from Reference 17. In the present study three discretization schemes for the convective part of the momentum equations are used at $Re = 20$ and 40. Results obtained using the QUICK and hybrid discretization schemes are in better agreement, while the upwind scheme fails to reproduce the correct peak values of pressure and wall vorticity. Two-dimensional plots of the velocity fields calculated using the QUICK scheme are shown in Figure 8 for $Re = 20$ and 40.

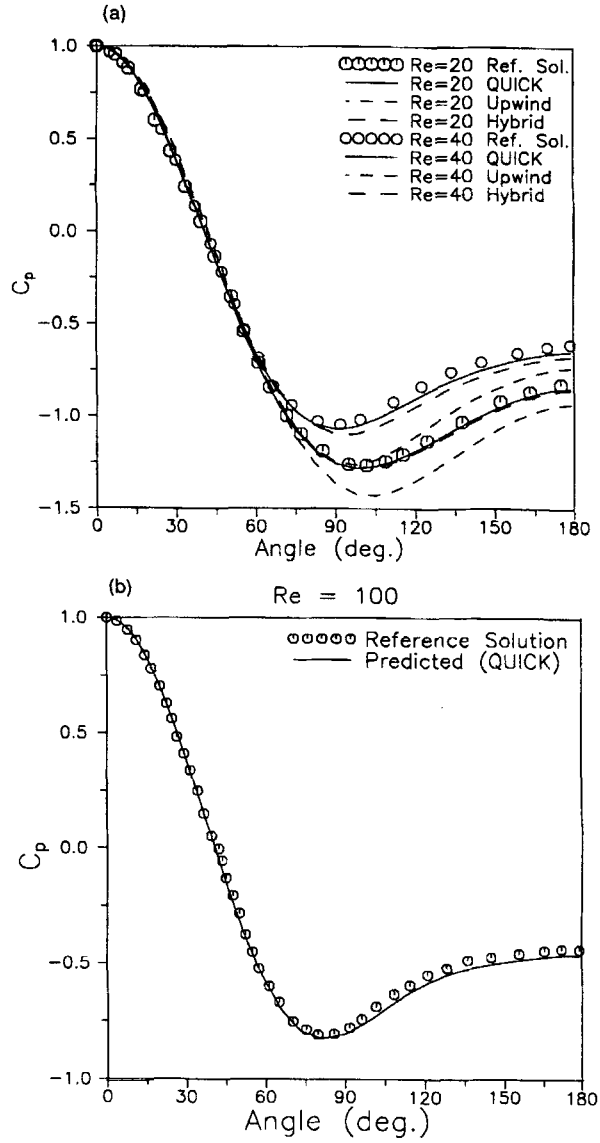

Figure 7. Pressure coefficient distribution along the cylinder surface: (a) $Re = 20$ and 40; (b) $Re = 100$

Figure 9 shows the convergence history for the $Re = 40$ case, demonstrating the excellent convergence properties of the proposed algorithm. Only the momentum equations were underrelaxed using $\omega = 0{\cdot}50$.

5.3. Laminar flow in a 90° bend of square cross-section

The proposed algorithm was also used for the numerical prediction of the three-dimensional developing laminar flow in a bend of 90° turning angle and square cross-section, for which experimental data are available.[18] The Reynolds number of the flow is 790 based on the bulk velocity

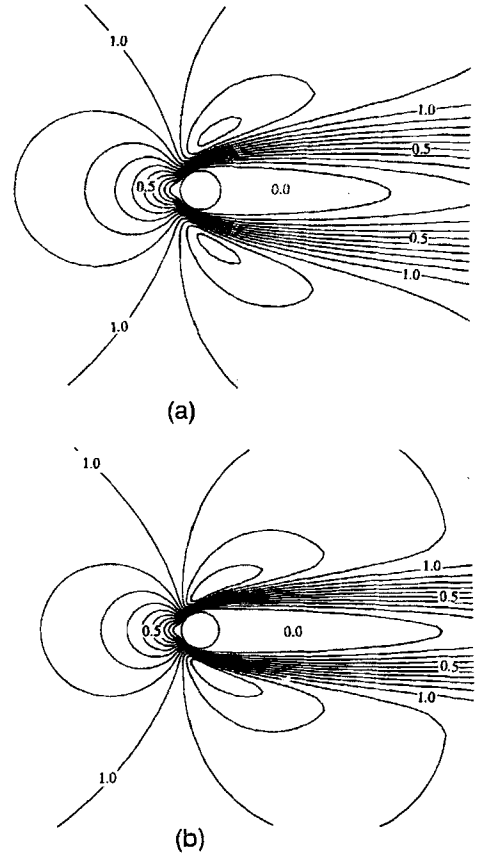

Figure 8. Velocity field around the cylinder: (a) $Re = 20$; (b) $Re = 40$

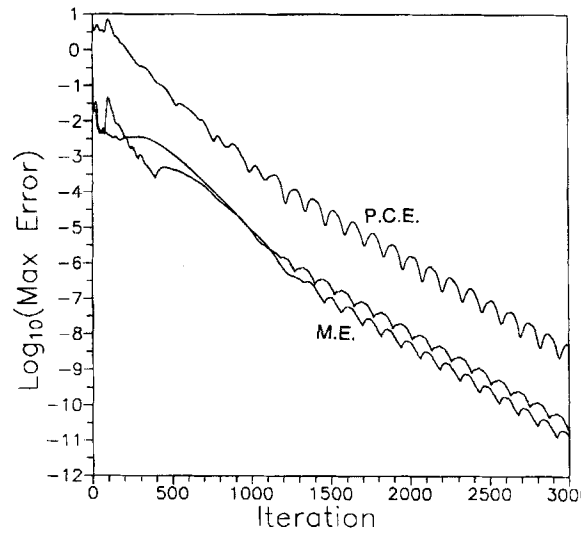

Figure 9. Convergence history for the flow around the cylinder, $Re = 40$, 101 × 101 grid nodes: P.C.E., pressure correction equation; M.E., momentum equations

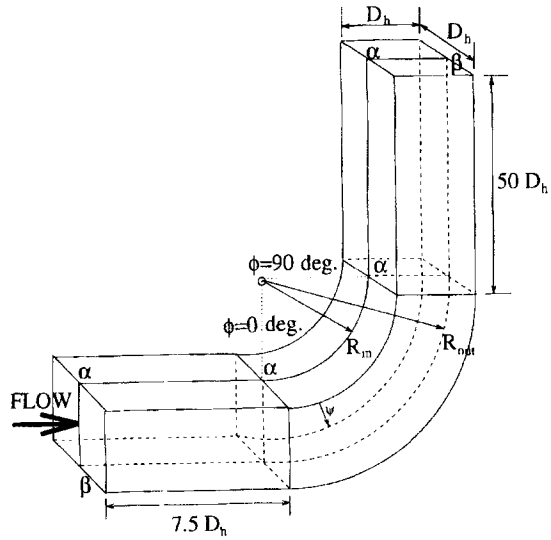

Figure 10. Perspective view of the 3D bend

and the hydraulic diameter D_h. A perspective view of the channel, along with useful notation, is shown in Figure 10. The flow is symmetric, allowing only half of the channel to be analysed. According to Figure 10, the Greek letters α and β are used to denote any edge lying on the symmetry plane, with α corresponding to the inner radius ($R_{in} = 0{\cdot}072$ m) and β denoting the outer radius ($R_{out} = 0{\cdot}112$ m) of the bend. The grid used consisted of 121 × 26 × 35 nodes in the streamwise, spanwise and radial directions respectively. Thirty-seven cross-planes were distributed inside the bend at equal angular distances, while the remaining planes covered the upstream and downstream straight extension parts.

A uniform velocity profile was imposed at the inlet plane located at a distance $8{\cdot}5D_h$ upstream of the entrance of the bend ($\phi = 0°$). Thus the calculation started one hydraulic diameter upstream of the real inlet plane of the experimental facility ($-7{\cdot}5D_h$), allowing the formation and development of a thin boundary layer which is very close to the experimental data at the subsequent measurement stations. A similar treatment was also used by other researchers.[19,20] Zero pressure level was imposed at the exit plane.

The calculated contours of the streamwise velocity component at various cross-sections upstream of, inside and downstream of the bend are shown in Figure 11. In the same figure the corresponding measured distributions are also plotted, with broken lines, in the lower half of each cross-section. As expected, the first planes reflect the effects of the imposed uniform inlet velocity profiles. Thus, as shown in Figures 11(a) and 11(b), the calculated flow acceleration is lower than the measured one. Further downstream the calculated and measured distributions are in satisfactory agreement; see Figures 11(c)–11(f). After the $\phi = 30°$ cross-section the flow is accelerated close to the inner radius wall owing to strong secondary flow effects. These effects could be identified in Figure 12, where the secondary velocity field over the $\phi = 90°$ cross-section is presented.

Figure 13 illustrates in more detail the streamwise velocity patterns at five cross-sections; for each cross-section, velocity profiles are presented in five radial positions, defined as

$$R = R_{out} - \psi(R_{out} - R_{in}),$$

where $\psi = 0{\cdot}1$, $0{\cdot}30$, $0{\cdot}50$, $0{\cdot}70$ and $0{\cdot}90$, spanning from the lower wall to the symmetry plane. The radial velocity component is presented in Figure 14 at the same spanwise transverses. This figure

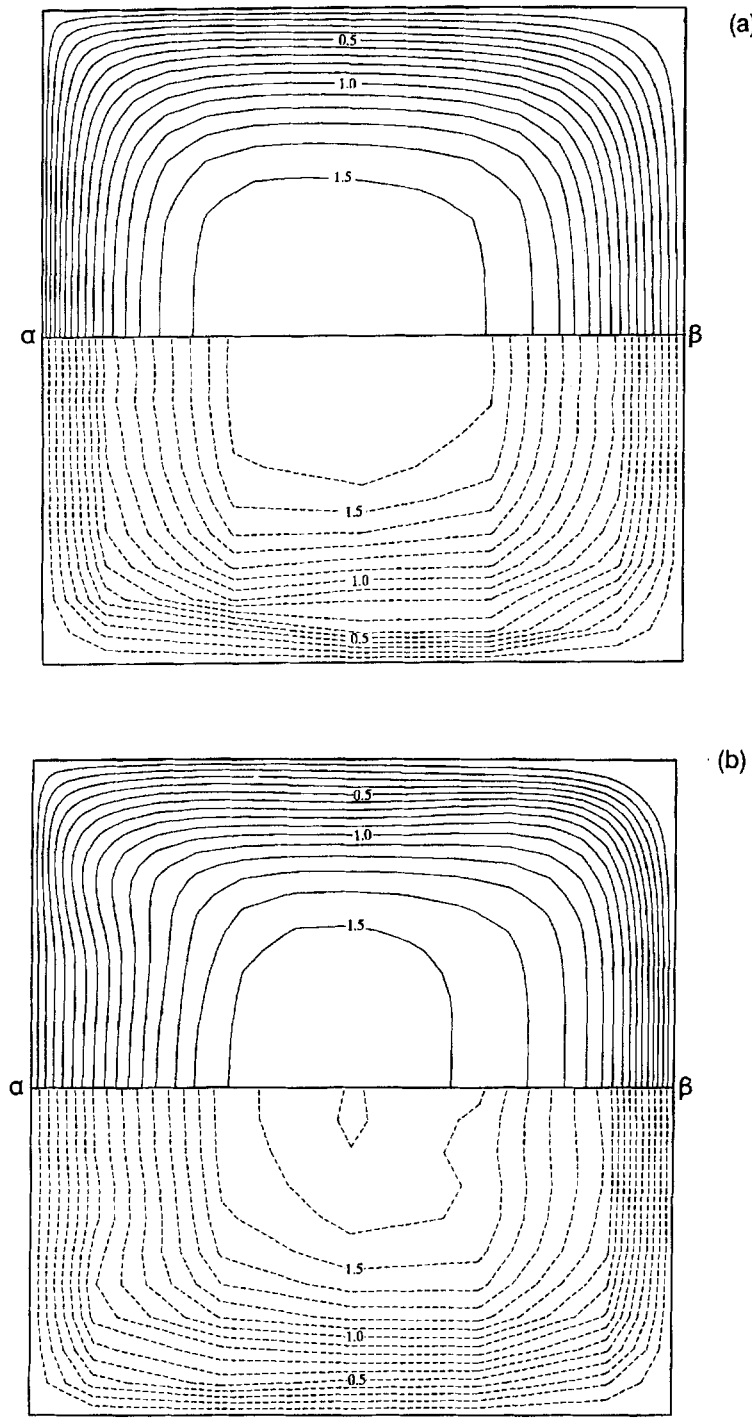

Figure 11. Calculated (upper half, full lines) and measured (lower half, broken lines) non-dimensional streamwise velocity component contours at various cross-planes: (a) $x = -0{\cdot}25D_h$; (b) $\phi = 30°$; (c) $\phi = 60°$; (d) $\phi = 77{\cdot}5°$; (e) $x = 0{\cdot}25D_h$; (f) $x = 2{\cdot}5D_h$

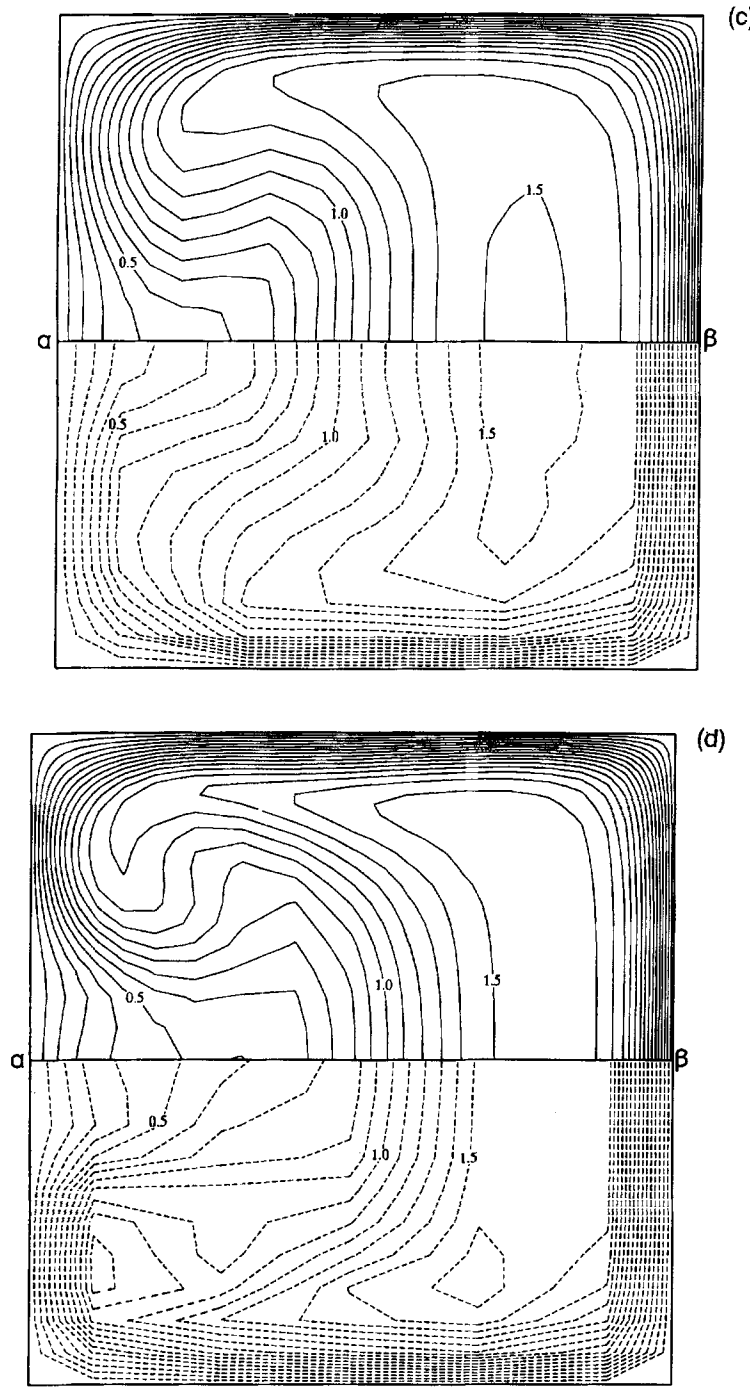

Figure 11. (*Continued*) Calculated (upper half, full lines) and measured (lower half, broken lines) non-dimensional streamwise velocity component contours at various cross-planes: (a) $x = -0{\cdot}25D_h$; (b) $\phi = 30°$; (c) $\phi = 60°$; (d) $\phi = 77{\cdot}5°$; (e) $x = 0{\cdot}25D_h$; (f) $x = 2{\cdot}5D_h$

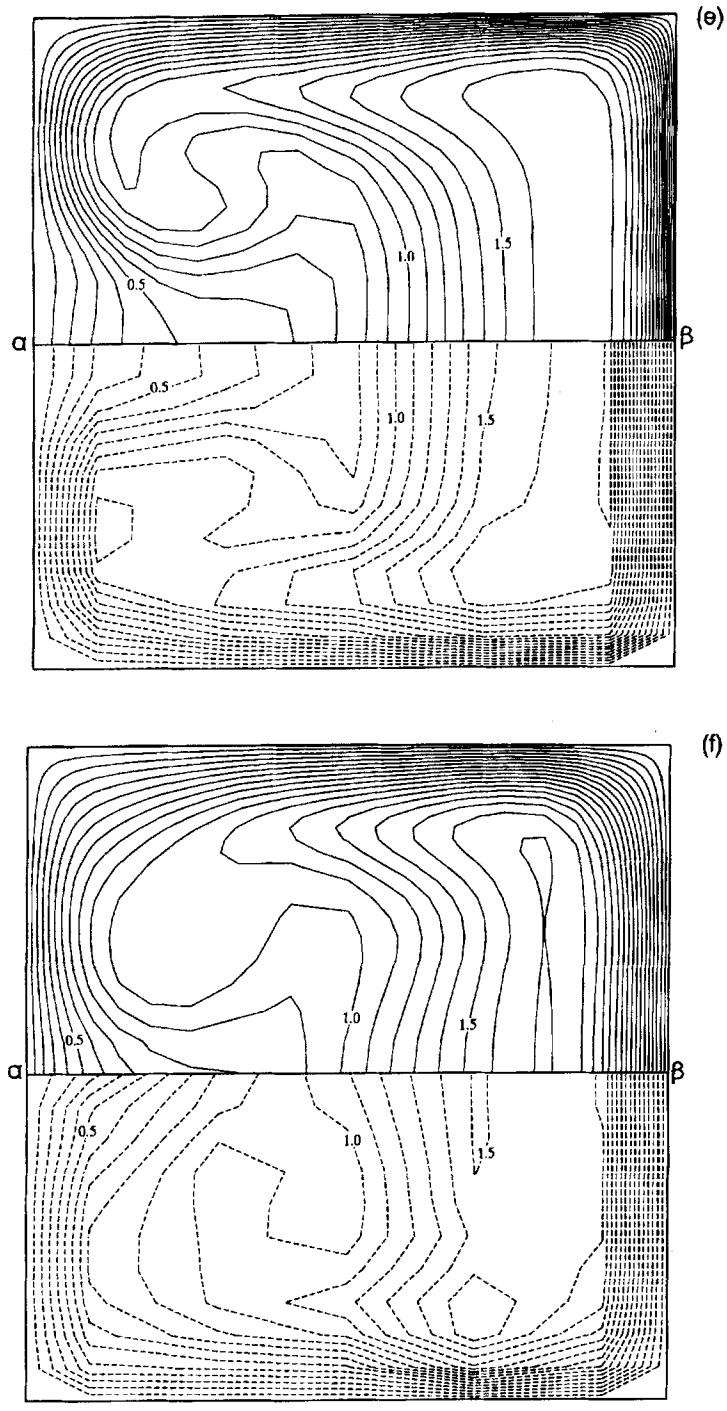

Figure 11. (*Continued*) Calculated (upper half, full lines) and measured (lower half, broken lines) non-dimensional streamwise velocity component contours at various cross-planes: (a) $x = -0{\cdot}25D_h$; (b) $\phi = 30°$; (c) $\phi = 60°$; (d) $\phi = 77{\cdot}5°$; (e) $x = 0{\cdot}25D_h$; (f) $x = 2{\cdot}5D_h$

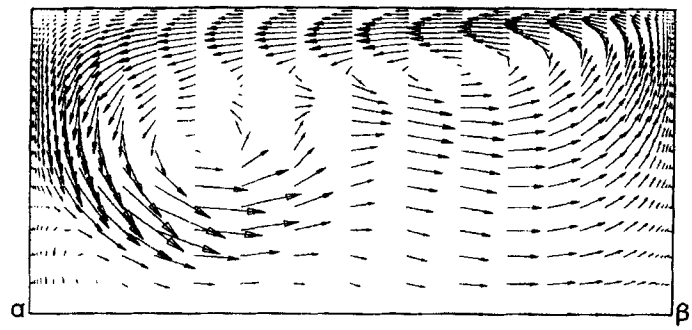

Figure 12. Secondary velocity field over the $\phi = 90°$ cross-section

certifies, from a different point of view, the previous conclusions. Both velocity components in Figures 11, 13 and 14 are non-dimensionalized by the bulk velocity.

Finally, the convergence history using Solver P2 for the pressure correction equation is shown in Figure 15. The pressure correction equation seems to behave as in the previously examined 2D cases and exhibits a monotonic convergence in the global sense. Owing to the 90° turning angle of the bend, two Cartesian velocity components are associated with the primitive flow direction. The momentum equations in these two directions present a convergence history which is very similar to that of the pressure correction equation. On the other hand the spanwise momentum equation also converges in a monotonic way but with unpredictable fluctuations around a mean value.

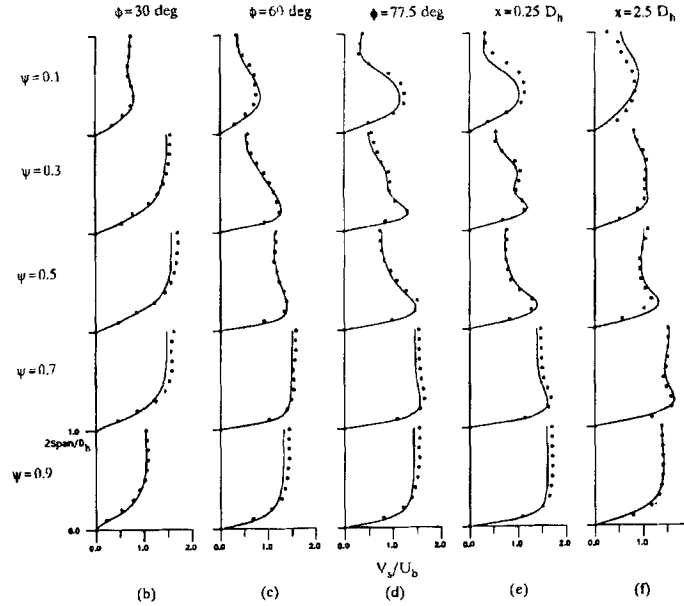

Figure 13. Calculated (full lines) and measured (symbols) non-dimensional streamwise velocity component profiles at various radial positions ψ and cross-planes: (b) $\phi = 30°$; (c) $\phi = 60°$; (d) $\phi = 77{\cdot}5°$; (e) $x = 0{\cdot}25D_h$; (f) $x = 2{\cdot}5D_h$

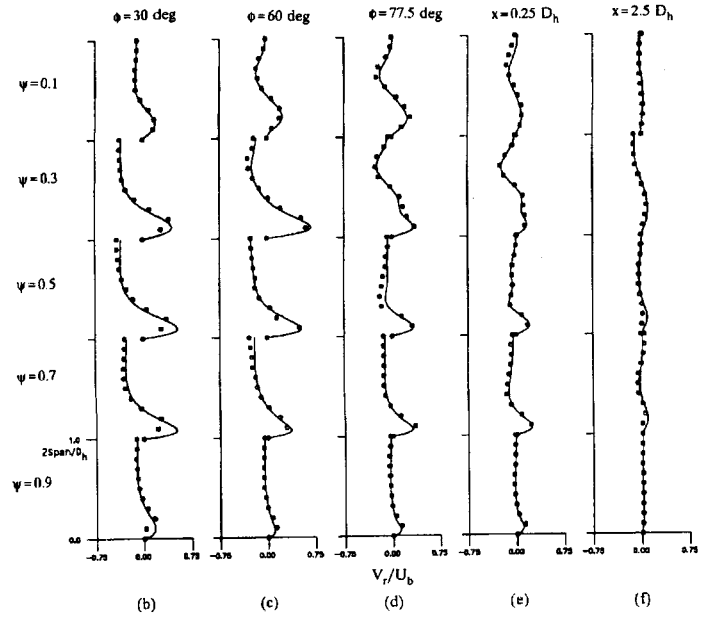

Figure 14. Calculated (full lines) and measured (symbols) non-dimensional radial velocity component profiles at various radial positions ψ and cross-planes: (b) $\phi = 30°$; (c) $\phi = 60°$; (d) $\phi = 77{\cdot}5$; (e) $x = 0{\cdot}25D_h$; (f) $x = 2{\cdot}5D_h$

For this case the CPU time per node per iteration was approximately 0·1 ms on an MIPS 8010 processor. The considerably low computational time is attributed to the fact that a single factorization (which is a time-consuming task) is carried out for all momentum equations. It must be pointed out that the required iteration number for practical calculations is much less than the one presented in the last figure, which renders the presented algorithm suitable for engineering computations.

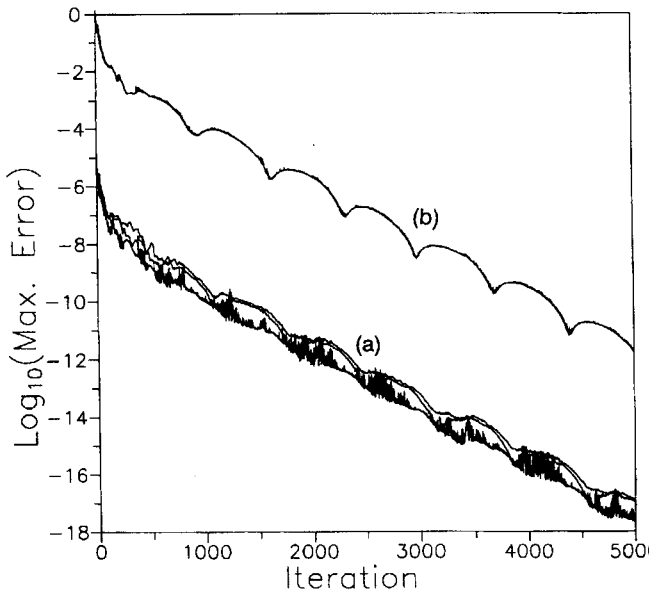

Figure 15. Convergence history for the 3D laminar flow in the bend: (a) momentum equations; (b) pressure correction equation

6. CONCLUSIONS

A solution method for laminar incompressible flows has been developed. It makes use of a segregated approach wherein the momentum and pressure correction equations are successively solved by means of fast elliptic solvers. It was demonstrated that the segregated approach can be economic in CPU time and efficient provided that appropriate implicit solvers are used for each equation. The modified strongly implicit procedure (MSIP) for scalar equations is proposed for the momentum equations. It is worth noting that the factorization process is paid once per iteration and that the convergence rate is insensitive to the value of the parameter α involved in the MSIP. A degenerated variant of the restarted preconditioned generalized minimal residual technique was used in place of the MSIP for the pressure correction equation and this accelerated convergence and improved reliability. The cost of using the preconditioned GMRES(1) algorithm turns out to be affordable thanks to the very small number of search directions; since the MSIP acts as preconditioner to the GMRES method, the factorization cost has to be paid in any case. The effect of moving all non-orthogonal cross-terms of the pressure correction equation in the RHS slows down the convergence rate but leads to faster iterations. Underrelaxation is important for the momentum equations but not for the pressure correction one. Best results were obtained when the QUICK scheme was used for the convective part of the momentum equations.

REFERENCES

1. A. J. Chorin, 'A numerical method for solving incompressible viscous flow problems', *J. Comput. Phys.*, **2**, 12–26 (1967).
2. G. V. Hobson and B. Lakshminarayana, 'Prediction of cascade performance using an incompressible Navier–Stokes technique', *ASME Paper 90-GT-261*, 1990.
3. W. Shyy, S. S. Tong and S. M. Correa, 'Numerical recirculating flow calculation using a body-fitted coordinate system', *Numer. Heat Transfer*, **8**, 99–113 (1985).
4. S. V. Patankar and D. B. Spalding, 'A calculation procedure for heat, mass and momentum transfer in three-dimensional parabolic flows', *Int. J. Heat Mass Transfer*, **15**, 1787–1806 (1972).
5. C. M. Rhie and W. L. Chow, 'Numerical study of the turbulent flow past an airfoil with trailing edge separation', *AIAA J.*, **21**, (1983).
6. G. E. Schneider and M. Zedan, 'A modified strongly implicit procedure for the numerical solution of field problems', *Numer. Heat Transfer*, **4**, 1–19 (1981).
7. Y. Saad and M. H. Schultz, 'GMRES: a generalized minimal residual algorithm for solving nonsymmetric linear systems', *Res. Rep. YALEU/DCS/RR-254*, Yale University, New Haven, CT, 1983.
8. S. V. Patankar, *Numerical Heat Transfer and Fluid Flow*, Hemisphere/McGraw-Hill, New York, 1978.
9. D. B. Spalding, 'A novel finite-difference formulation for differential expressions involving both first and second derivatives', *Int. j. numer. methods eng.*, **4**, 551 (1972).
10. B. P. Leonard, 'A stable and accurate convective modelling procedure based on quadratic upstream interpolation', *Comput. Methods Appl. Mech. Eng.*, **19**, 59–98 (1979).
11. T. Hayase, J. A. C. Humphrey and R. Greif, 'A consistently formulated QUICK scheme for fast and stable convergence using finite-volume iterative calculation procedures', *J. Comput. Phys.*, **98**, 108–118 (1992).
12. S. Majumdar, 'Role of underrelaxation in momentum interpolation for calculation of flow with nonstaggered grids', *Numer. Heat Transfer*, **13**, 125–132 (1988).
13. M. Peric, 'Analysis of pressure–velocity coupling on nonorthogonal grids', *Numer. Heat Transfer B*, **17**, 63–82 (1990).
14. M. Napolitano and P. Orlandi, 'Laminar flow in a complex geometry: a comparison', *Int. j. numer. methods fluids*, **5**, 667–683 (1985).
15. K. A. Cliffe, C. P. Jackson and A. C. Greenfield, 'Finite-element solutions for flow in a symmetric channel with a smooth expansion', *AERE-R 10608*, 1983.
16. A. S. Grove, F. H. Sharir, E. E. Petersen and A. Acrivos, 'An experimental investigation of the steady separated flow past a circular cylinder', *J. Fluid Mech.*, **19**, 60–80 (1964).
17. B. Fornberg, 'A numerical study of steady viscous flow past a circular cylinder', *J. Fluid Mech.*, **98**, 819–855 (1980).
18. A. M. K. P. Taylor, J. H. Whitelaw and M. Yianneskis, 'Measurements of laminar and turbulent flow in a curved duct with thin inlet boundary layers', *NASA Contractor Rep. 3367*, 1981.
19. F. Sotiropoulos and V. C. Patel, 'Flow in curved ducts of varying cross-section', *IIHR Rep. 358*, 1992.
20. T. R. Govindan, W. R. Briley and H. McDonald, 'General three-dimensional viscous primary/secondary flow analysis', *AIAA J.*, **29**, (1991).